Enhanced Photoelectrochemical Performance in Reduced Graphene Oxide/$BiFeO_3$ Heterostructures

Yan Ren, Feng Nan, Lu You, Yang Zhou, Yanyan Wang, Junling Wang, Xiaodong Su, Mingrong Shen, and Liang Fang**

***B**iFeO$_3$ (BFO)-based ferroelectrics have been proved to be visible-light-driven photoelectrodes for O_2 production. However, the hitherto reported photoelectrochemical performances remain inferior to meet the requirements for any applications. Besides, expensive noble metals (Ag, Au) are commonly required to achieve high photoelectric conversion efficiency. Here, the significant enhancements of photoelectrochemical performance is reported by fabricating a noble-metal-free reduced graphene oxide (RGO)/BFO composite film via a simple and cost-effective solution process. The optimized RGO/BFO composite film exhibits a 600% improvement of the short-circuit photocurrent density compared to that of the pristine BFO, and also outperforms the noble-metal/BFO cells under the same reaction conditions. Furthermore, the incident photon-to-current efficiency of the optimized RGO/BFO sample shows threefold enhancement. This study delivers a facile and low-cost approach to preparing 2D materials/ferroelectric heterostructures and offers a promising pathway to boost the performance of semiconducting ferroelectric photoelectrodes.*

1. Introduction

The demand for harvesting clean and renewable energy from sunlight has triggered intensive research in semiconductor thin film for solar cell, water splitting, and environmental remediation applications. Of particular interest is the photoelectrochemical (PEC) water splitting technique,[1,2] which converts light energy into chemical and electrical energies. However, the short carrier diffusion length and poor charge transport property of semiconductor photoelectrode still limit the efficiency in PEC cells.

Owing to the revived interest in ferroelectric photovoltaic effect,[3–5] narrow-bandgap ferroelectrics have recently emerged as potential photoelectrodes in PEC cells.[6–8] In contrast to conventional semiconductor-based solar cells, ferroelectric cells exhibit some unique features, such as switchable photovoltaic outputs,[9–13] above-bandgap photovoltage,[14–16] and above-Shockley–Queisser-limit efficiency.[17] However, the microscopic mechanism of the ferroelectric photovoltaic effect remains to be reconciled. While bulk photovoltaic effect based on the shift current model is believed to govern the photoresponse in large-scale single crystals and ceramics,[18,19] the behaviors of thin-film ferroelectric capacitors are better explained by the polarization-mediated interfacial band bending.[11,20] Furthermore, defects such as oxygen vacancies are ubiquitous in perovskite oxides,[21,22] and their effects on photovoltaic performance remain to be clarified.[23]

Multiferroic $BiFeO_3$ (BFO) with robust room-temperature ferroelectricity and a bandgap (≈2.7 eV) within visible light

Y. Ren, Dr. F. Nan, Dr. Y. Wang, Prof. X. Su, Prof. M. Shen, Prof. L. Fang
College of Physics
Optoelectronics and Energy and Jiangsu Key Laboratory of Thin Films
Soochow University
Suzhou 215006, P. R. China
E-mail: lfang@suda.edu.cn

Dr. L. You, Dr. Y. Zhou, Prof. J. Wang
School of Materials Science and Engineering
Nanyang Technological University
Singapore 639798, Singapore
E-mail: youlu@ntu.edu.sg

DOI: 10.1002/smll.201603457

range, stands out as a candidate material for PEC study. Different from the powder PEC system, the PEC thin film cells greatly facilitate the fabrication process and the direct investigation of the effect of ferroelectric polarization on PEC properties. The early study on BFO polycrystalline films showed that improving film crystallinity could reduce the dark current and enhance the photocurrent density.[24] Subsequently, Ji et al. observed significant anodic photocurrent in the epitaxial BFO films,[25] but the ferroelectric polarization only slightly affected the PEC properties. In contrast, Cao et al. reported strong polarization-dependent PEC responses in BFO polycrystalline films.[26]

Although BFO films can be used as photoelectrodes in a PEC system, the performances remain poorly rated due to the rapid recombination of photogenerated electrons and holes. There has been an explosion of interest in improving PEC performance of BFO epitaxial or polycrystalline films. For example, Cho et al. utilized a pulsed laser deposition technique to synthesize BFO-$SrTiO_3$ solid-solution epitaxial films with good structural and PEC properties.[27] Quynh et al. also used the same method to fabricate BFO/ε-Fe_2O_3 vertical-heteroepitaxy films,[28] and found that the photocurrent density was much larger than that of the pure BFO. Recently, our group demonstrated that by decorating the BFO surface with appropriate amount of Ag nanoparticles, the maximum short-circuit photocurrent density could be doubled.[29]

In pursuit of novel device paradigm to enhance PEC effect of semiconductors, the noble-metal-free graphene-based nanocomposite system has attracted much attention.[30] Owing to the abundance of delocalized electrons from the conjugated sp^2-bonded carbon network, graphene enhances the transport of photogenerated electrons in semiconductor photoelectrodes, which can increase the efficiency of the PEC system.[31] However, it is difficult to make graphene well dispersed in water due to its hydrophobicity. Although graphene oxide (GO) with rich hydrophilic groups has greatly eased the synthesis of composite materials due to its stable and high dispersion in water, the conductivity of GO is relatively low. Therefore, reduced graphene oxide (RGO), as an intermediate state between graphene and GO, offers an opportunity for fabrication of composite photoelectrodes.[32]

In this study, the polycrystalline BFO film is fabricated by a sol–gel method, and the RGO nanosheets are then decorated on top of the BFO film through a dip-coating method. The influence of RGO on the properties of BFO is systematically investigated, and remarkable enhancement of PEC performance is achieved using the BFO decorated with RGO nanosheets as the photoelectrode. Furthermore, a mechanism for PEC reaction in the RGO/BFO system is proposed. This study opens up a new pathway toward the enhancement of the PEC effect of ferroelectric films, which are promising candidates for clean energy applications.

2. Results and Discussion

The morphologies and the thicknesses of the RGO nanosheets were measured by atomic force microscopy (AFM). **Figure 1**a,b shows RGO nanosheets with lateral dimensions of 100–500 nm and heights in the range of

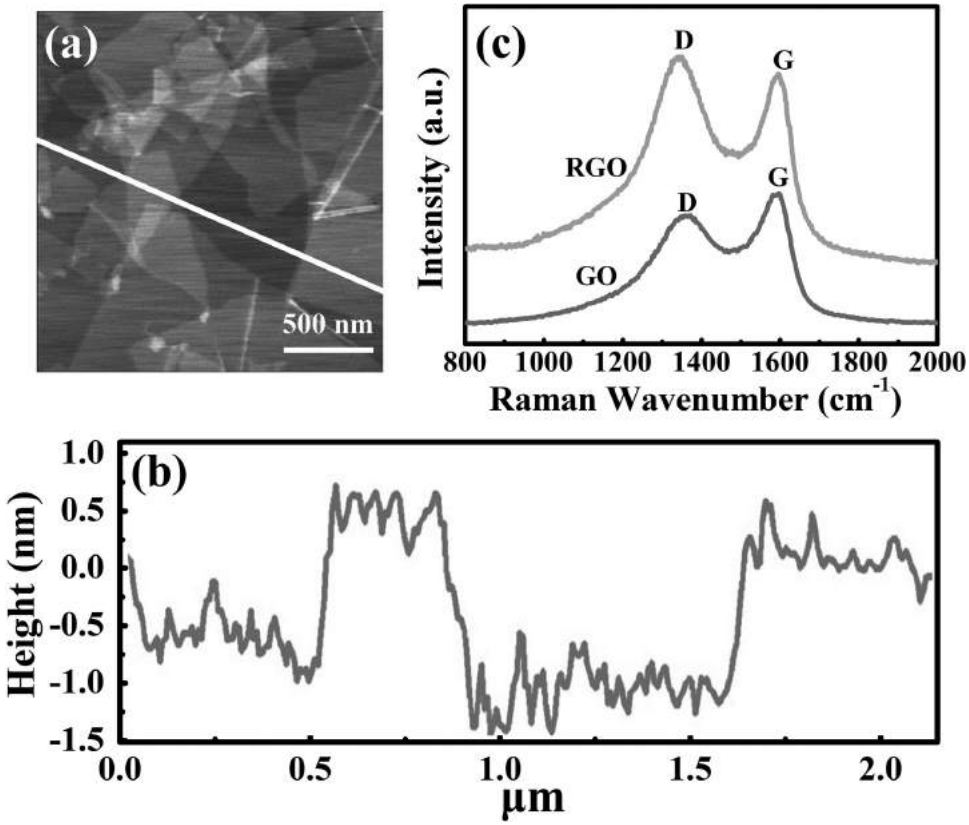

Figure 1. a) AFM image, b) the section analysis of the RGO nanosheets, and c) Raman scattering spectra of GO and RGO.

1.3 ± 0.2 nm, confirming the monolayer nature.[33] Because of its high sensitivity to the lattice vibrational modes of carbon nanomaterials, Raman spectroscopy provides valuable information in graphene characterization, especially in terms of chemical functionalization. Figure 1c illustrates the comparison of the Raman spectra of GO and RGO. There are two prominent Raman scattering peaks centered at 1356 and 1608 cm^{-1}, which can be attributed to D and G bands, respectively. Clearly, the D/G intensity ratio of RGO is higher than that of GO, as the result of the restoration of sp^2-hybridized carbon during the reduction reaction.[34]

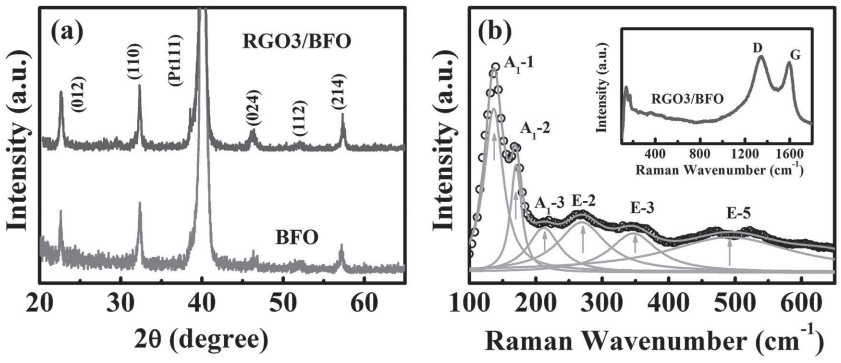

Figure 2. a) XRD patterns of the pure BFO and RGO3/BFO films; b) Raman scattering spectra of the RGO3/BFO films (measured spectra: open circles, fitted spectra: thick solid lines) and the decomposed active modes (thin solid lines and arrows). Inset shows the Raman scattering spectra of the RGO3/BFO films.

The crystal structures of the BFO thin film before and after RGO decoration were measured by X-ray diffraction (XRD), as shown in **Figure 2**a. Both XRD patterns exhibit clear and identical diffraction peaks, which can be indexed according to the rhombohedral structure of BFO (JSPDS file No. 21–1272). To verify the microscopic ferroelectric properties of the BFO film, piezoresponse force microscopy (PFM) was employed. Both a tip-writing box-in-box pattern and local switching hysteresis loop demonstrate the switchable characteristic of the ferroelectric polarization of the BFO film (Figure S2, Supporting Information). Since the RGO concentration is too small in the composite film, no XRD peak of RGO can be detected. Raman spectroscopy was performed again to confirm the existence of RGO. As shown in the inset of Figure 2b, two prominent peaks corresponding to D and G bands of RGO are clearly identified in the RGO3/BFO composite film. Furthermore, some additional peaks can be observed in the wavelength range from 100 to 600 nm, which can be attributed to BFO phase (Figure 2b). In order to clarify the Raman active modes of these peaks, the measured spectrum was fitted by decomposing into individual Lorentzian components. Two peaks with strong scattering intensities and four peaks with medium scattering intensities can be attributed to A_1-1 (137 cm^{-1}), A_1-2 (170 cm^{-1}), A_1-3 (213 cm^{-1}), E-2 (270 cm^{-1}), E-3 (344 cm^{-1}), and E-5 (473 cm^{-1}) modes, respectively. These results are in good agreement with those of the BFO epitaxial films or nanoparticles in terms of relative scattering intensities and mode frequencies.[35,36] From the above analyses, we can conclude that the desired RGO/BFO composite films have been achieved.

Figure 3a shows the typical UV–vis absorption spectra of the BFO before and after decorated with the RGO nanosheets. The pure BFO film shows the characteristic spectrum with its fundamental absorption edge rising at 460 nm, while the RGO3/BFO sample shows better light absorption capability in the whole visible-light range due to the presence of RGO. In addition, the RGO3/BFO sample displays the same absorption edge as that of BFO, which implies the carbon in the RGO3/BFO sample is free graphitic carbon.[37] Ultraviolet photoelectron spectroscopy (UPS) was then used to measure the band edges of the BFO thin film, as shown in Figure 3b. The work function (ϕ) calculated by subtracting the spectrum width from the photon energy of exciting radiation (21.2 eV) is determined to be 5.61 eV for the BFO film. The energy level of E_F–E_V is 1.12 eV, which is derived by extrapolating the linear portion of the low binding energy edge of the peak to the energy axis. Based upon the above values and the bandgap of the BFO film (2.46 eV, calculated from Tauc's equation based on absorption spectra), the energy band diagram is schematically shown in the inset of Figure 3a, which demonstrates that the BFO film in this study can be regarded as a p-type semiconductor.

To evaluate the PEC performance of the photoelectrodes, the short-circuit photocurrent densities versus time for the different RGO/BFO photoelectrodes were investigated. As shown in **Figure 4**a, all samples exhibit prompt and reproducible cathodic photocurrent density. The negative value of the photocurrent is consistent with the p-type semiconducting behavior of BFO.[7,27] A photocurrent density of ≈–15 μA cm^{-2} at 0 V versus Ag/AgCl can be observed in the pure BFO film. By adding more RGO nanosheets, the photocurrent density of the composite film increases and reaches a maximal

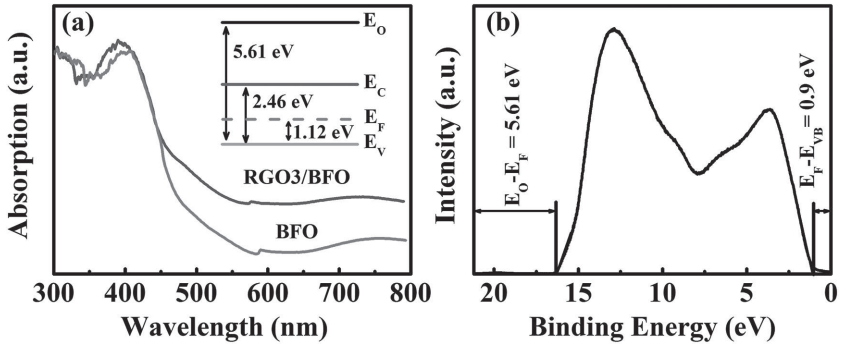

Figure 3. a) The UV–vis absorption of the pure BFO and RGO3/BFO films. Inset shows the schematic diagrams illustrating the energy band alignment of BFO. E_O, E_F, E_V, and E_C represent vacuum level, Femi level, valence band, and conduction band of BFO, respectively. b) UPS spectrum of the pure BFO films.

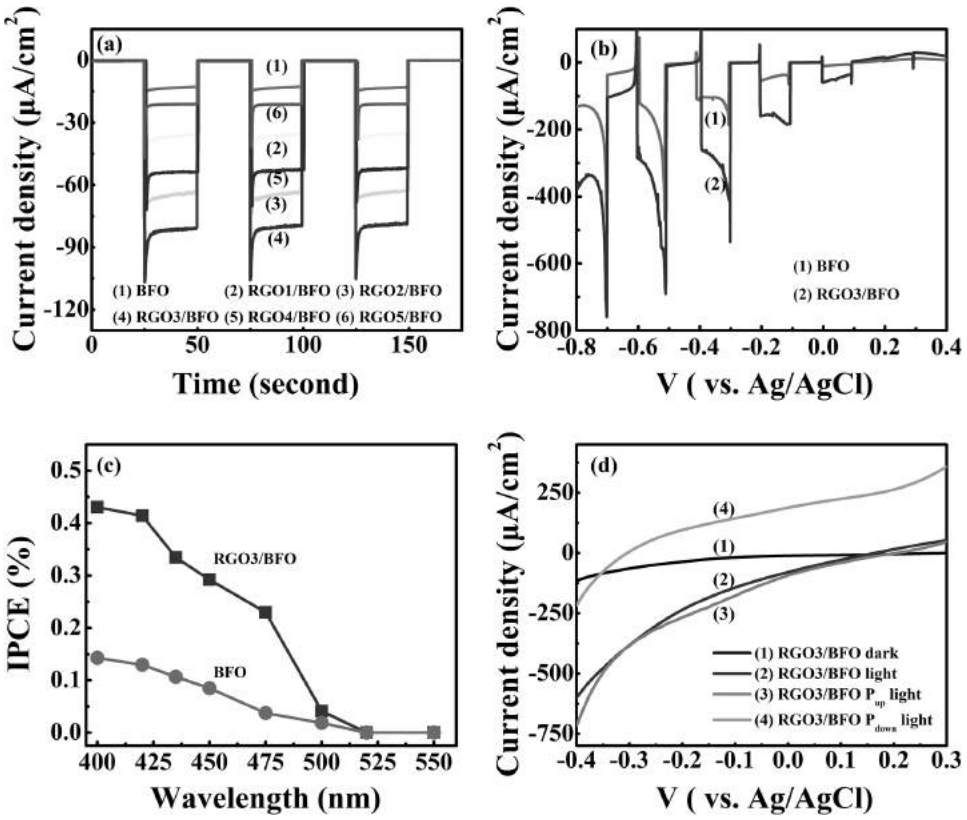

Figure 4. a) The short-circuit photocurrent densities versus time for the different RGO/BFO photoelectrodes; b) the function of photocurrent density with applied voltage under chopped illumination for the different samples; c) IPEC enhancement factor as a function of the wavelength for the different samples at 0 V versus Ag/AgCl; and d) linear sweep voltammetry curves of the RGO3/BFO films with different ferroelectric polarization directions.

value in the RGO3/BFO film (≈–90 μA cm^{-2} at 0 V vs Ag/AgCl). This value is higher than the current density reported for BFO epitaxial films or polycrystalline films,[24,25,38,39] and also surpasses that of BFO decorated with noble-metal Au, Ag, or Pd nanoparticle.[40–43] Further increase of RGO nanosheets content leads to the reduction of photocurrent density. The initial increase of photocurrent density can be ascribed to the increased content of RGO nanosheets, which enhances the separation of photogenerated carriers. However, the higher coverage of RGO nanosheets reduces the surface area of BFO in direct contact with the electrolyte, and decreases the intensity of light absorbed by the BFO film.[44]

Figure 4b shows the linear sweep voltammetry (J–V) curves under chopped illumination for the BFO and RGO3/BFO samples. There is a steady increase in photocurrent density with increasing applied potential, and a fast photocurrent response is observed for each switch on and switch off event for both samples. In addition, both samples exhibit current transients (spikes) during the potential scan under the illumination condition. This behavior has been attributed to the generation and recombination dynamics of charge carriers in the photoanodes before reaching steady-state kinetics.[45] The RGO3/BFO sample shows a much stronger response as compared with that of BFO, confirming the superiority of the former in photoenergy conversion. For example, the photocurrent density of the RGO3/BFO sample is ≈–160 μA cm^{-2} at –0.2 V versus Ag/AgCl, which is also higher than that reported for the BFO polycrystalline film with 2% Ag (–70 μA cm^{-2} at –0.2 V vs Ag/AgCl),[46] and higher than BFO/ε-Fe_2O_3 vertical heteroepitaxy films (190 μA cm^{-2} at 0.6 V vs Ag/AgCl).[28] Compared with these studies, our RGO/BFO composite photoelectrodes not only show superior PEC performance, but also exhibit the advantage of the low-cost and simple fabrication process.

The incident photo-to-current conversion efficiency (IPCE) was also measured to verify the effect of the RGO nanosheets, as shown in Figure 4c. The IPCE measurement for all the samples mainly covers the wavelength range of 400–550 nm, which matches well with the absorption spectrum of BFO. Both samples demonstrate a photocurrent density onset at 520 nm corresponding to the bandgap of BFO. Since the enhanced light absorption of the RGO/BFO film is in the range larger than 450 nm, the onset measured in IPCE implies that the photocurrent generation only occurs for above-bandgap photoexcitation of BFO, thus excluding the possible photocurrent contribution due to the photoexcitation in RGO. The IPCE value of the pure BFO film is 0.15% (at 400 nm), whereas the IPCE response shows a remarkable enhancement to 0.43% when RGO is incorporated. We also investigate the relationship between the PEC performance and the ferroelectric polarization in the RGO3/BFO sample. As shown in Figure 4d, the RGO3/BFO photoelectrode shows the switchable PEC properties. The onset potential is ≈0.08 V and the short-circuit photocurrent density is ≈–90 μA cm^{-2} with the upward polarization, which are similar to those values of the as-grown sample.

On the contrary, the signs of the onset potential (≈–0.36 V) and the short-circuit photocurrent density (≈150 μA cm^{-2}) are reversed with the downward polarization. Such phenomena can be attributed to the polarization-mediated band bending effect commonly observed in ferroelectric heterojunctions.[29]

In order to gain deeper insight into the charge-transfer process of the PEC cell, electrochemical impedance spectroscopy (EIS) was carried out without illumination. **Figure 5**a shows the Nyquist plots of the pure BFO and RGO3/BFO photoelectrodes. In each case, only one arc on the EIS plane can be observed, suggesting that the surface charge-transfer process dominates in the PEC reaction. In general, the arc radius of the Nyquist plots reflects the reaction rate occurring at the surface of the electrode.[47] The arc radius of the RGO3/BFO sample is much smaller than that of the pure BFO sample, indicating a faster interfacial charge transfer to the electrode donor/electron acceptor and an effective separation of photogenerated carriers as suggested. From the IPCE and EIS results, we can conclude that the photocarrier separation and the charge-transfer process play a more important role compared to the light absorption in our system.

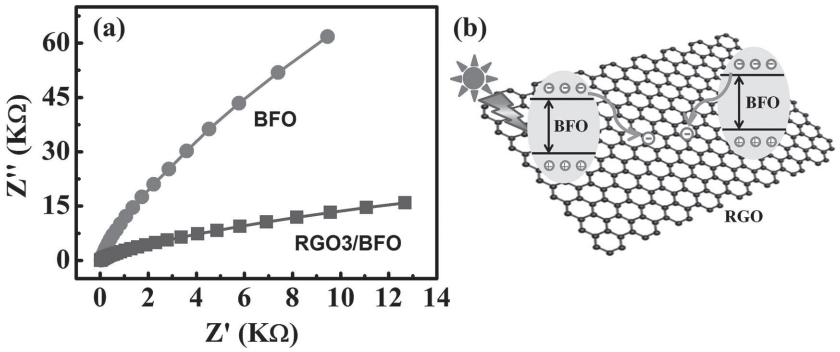

Figure 5. a) EIS Nyquist plots of the pure BFO and RGO3/BFO films without light irradiation; b) schematic illustration for the charge transfer and separation in the RGO/BFO system.

On the basis of the physical and electrochemical characterizations, a mechanism was proposed to explain the enhanced photoelectrochemical properties of RGO/BFO (Figure 5b). Besides the light absorption, the charge transportation and separation were also considered to be key factors on improving the photoelectronchemical activity. RGO has been reported to be a competitive candidate for the acceptor material due to the unique delocalized conjugated structure and superior electrical conductivity. Previous study demonstrated that the excited electrons of TiO_2 or ZnO could transfer from the semiconductor conduction band to RGO via a percolation mechanism.[48,49] Similarly, in the present work, the photogenerated electrons would transfer from the conduction band of BFO to RGO, and the RGO serves as an acceptor of electrons and suppresses charge recombination effectively,[50] resulting in higher photocurrent density.

In addition to the suppression of the carrier recombination, other factors may also facilitate the photoelectrochemical reaction, such as photoexcited long-lifetime hot electron injection from BFO into RGO and possibly a better-matched band alignment between RGO and the electrolyte. Future studies are required to form a better understanding of the underpinning physics. Nevertheless, the combination of photoactive ferroelectrics and electrically benign 2D materials represents a novel device paradigm in PEC field and warrants more research focus.

3. Conclusion

In summary, the RGO/BFO composite photoelectrode was prepared by the sol–gel method followed by the dip-coating method. After the optimization of the RGO nanosheets content, we obtain a significant enhancement of photocurrent density as well as IPCE in the hybrid PEC cells. It is believed that the delocalized conjugated structure and superior electrical conductivity of RGO facilitate the electron injection from BFO, consequently suppressing the photogenerated electron–hole recombination, and eventually leading to the enhanced PEC performance. This work creates a green and simple way to enhance the PEC performance of ferroelectric photoelectrodes by incorporating 2D materials.

4. Experimental Section

Preparation of RGO/BFO Photoelectrode: The BFO thin films were prepared by the sol–gel method. $Bi(NO_3)_3{\cdot}5H_2O$ and $Fe(NO_3)_3{\cdot}9H_2O$ were dissolved in 2-methoxyethanol, and stabilized by adding citric acid. The solution was spin-coated onto Pt/Ti/SiO_2/Si(100) substrate for PEC measurement, and onto FTO substrate for optical absorption measurement. The wet films were dried at 200 °C in air for 2 min, followed by 400 °C for 5 min. This coating process was repeated to obtain a film thickness of 200 nm. Finally, the films were annealed at 640 °C in O_2 for 2 h. Dried GO powder (100 mg) prepared by a modified Hummer's method[51] was suspended in distilled water (100 mL) with stirring and ultrasoncation at least for 1 h. Reduction was carried out by hydrazine hydrate (the weight ratio of hydrazine hydrate/GO = 1) at 100 °C for 24 h. Stirring and ultrasonication were also used throughout the whole preparation process. Subsequently, the RGO powder was isolated via filtration, and washed with distilled water for four times.[52,53] Finally, such powder was dried at 60 °C for 24 h to remove residual solvent. The RGO/BFO composite films were then prepared by a dip-coating method: appropriate as-prepared RGO was dispersed in distilled water to form a 0.1 mg L^{-1} dispersion, 10 μL RGO aqueous suspension was then dip-coated onto the surface of the BFO films. The schematic diagram of the RGO/BFO composite photoelectrode is shown in Figure S1a in the Supporting Information. In addition, to investigate the effect of the RGO concentration on the PEC properties, the dip-coating process was repeated at 0, 1, 2, 3, 4, and 5 times, respectively. The samples were designated as BFO, RGO1/BFO, RGO2/BFO, RGO3/BFO, RGO4/BFO, and RGO5/BFO, respectively.

Characterization: The morphology and PFM measurements were carried out on a commercial atomic force microscope

(MFP-3D, Asylum Research) using Pt/Ir-coated tips. Raman spectra were taken at room temperature with a JY-HR800 Raman spectrometer operating at a wavelength of 514.5 nm as the excitation source. The structure of the films was analyzed using an XRD diffractometer (Rigaku D/MAX 3C) equipped with Cu Kα radiation (λ = 1.540598Å). The optical absorption spectra of the films were measured using a UV–vis–NIR spectrometer (Perkin Elmer Lambda 750). UPS measurement was conducted using a ESCALAB 250xi X-ray photoelectron spectrometer (ThermoFisher Scientific) with Helium I (21.21 eV) as the radiation source.

PEC Measurements: Photocurrent density and electrochemical impedance spectroscopy (EIS) measurements were obtained by using electrochemical analyzer (CHI-660D, Shanghai Chenhua Instrument Co. Ltd.) in a standard three-electrode configuration, as shown in Figure S1b in the Supporting Information. The film, a Pt wire, and an Ag/AgCl electrode were used as the working, counter, and reference electrodes, respectively. 0.1 M Na_2SO_4 aqueous solution was used as the electrolyte. The light source was a 300 W Xe lamp with tunable light intensity, calibrated using a Newport 1918-C photometer. The Nyquist plot was obtained using an AC voltage of 10 mV with a frequency range of 0.01 Hz to 10 MHz. To study the effect of the ferroelectric polarization on the PEC properties, the RGO/BFO film was macroscopically poled in an electrochemical cell containing three electrodes and aqueous electrolyte (0.1 M Na_2SO_4).[54] Potentials of +8 V and −8 V were applied on the Ag/AgCl electrode, and the polarization pointing away (toward) the substrate is defined as upward (downward) polarization, abbreviated as P_{up} (P_{down}). During the poling procedure, the current was kept below 1 mA.

Supporting Information

Supporting Information is available from the Wiley Online Library or from the author.

Acknowledgements

Y.R. and F.N. contributed equally to this work. This work was supported by the National Natural Science Foundation of China (Grant No. 51302179), the Natural Science Foundation of Jiangsu Province (Grant No. BK20131163), and the Priority Academic Program Development of Jiangsu Higher Education Institutions (PAPD).

[1] A. Fujishima, K. Honda, *Nature* **1972**, *238*, 37.
[2] M. G. Walter, E. L. Warren, J. R. McKone, S. W. Boettcher, Q. X. Mi, E. A. Santori, N. S. Lewis, *Chem. Rev.* **2010**, *110*, 6446.
[3] Y. B. Yuan, Z. G. Xiao, B. Yang, J. S. Huang, *J. Mater. Chem. A* **2014**, *2*, 6027.
[4] K. T. Butler, J. M. Frost, A. Walsh, *Energy Environ. Sci.* **2015**, *8*, 838.
[5] C. Paillard, X. Bai, I. C. Infante, M. Guennou, G. Geneste, M. Alexe, J. Kreisel, B. Dkhil, *Adv. Mater.* **2016**, *28*, 5153.
[6] M. Rioult, S. Datta, D. Stanescu, S. Stanescu, R. Belkhou, F. Maccherozzi, H. Magnan, A. Barbier, *Appl. Phys. Lett.* **2015**, *107*, 103901.
[7] S. Li, B. AlOtaibi, W. Huang, Z. Mi, N. Serpone, R. Nechache, F. Rosei, *Small* **2015**, *11*, 4018.
[8] Z. J. Wang, D. W. Cao, L. Y. Wen, R. Xu, M. Obergfell, Y. Mi, Z. B. Zhan, N. Nasori, J. Demsar, Y. Lei, *Nat. Commun.* **2016**, *7*, 10348.
[9] T. Choi, S. Lee, Y. J. Choi, V. Kiryukhin, S. W. Cheong, *Science* **2009**, *324*, 63.
[10] W. Ji, K. Yao, Y. C. Liang, *Adv. Mater.* **2010**, *22*, 1763.
[11] L. Fang, L. You, Y. Zhou, P. Ren, Z. S. Lim, J. Wang, *Appl. Phys. Lett.* **2014**, *104*, 142903.
[12] R. Nechache, C. Harnagea, S. Li, L. Cardenas, W. Huang, J. Chakrabartty, F. Rosei, *Nat. Photonics* **2015**, *9*, 61.
[13] Y. Yuan, T. J. Reece, P. Sharma, S. Poddar, S. Ducharme, A. Gruverman, Y. Yang, J. Huang, *Nat. Mater.* **2011**, *10*, 296.
[14] S. Y. Yang, J. Seidel, S. J. Byrnes, P. Shafer, C. H. Yang, M. D. Rossell, P. Yu, Y. H. Chu, J. F. Scott, J. W. Ager III, L. W. Martin, R. Ramesh, *Nat. Nanotechnol.* **2010**, *5*, 143.
[15] M. Alexe, D. Hesse, *Nat. Commun.* **2011**, *2*, 256.
[16] A. Bhatnagar, A. R. Chaudhuri, Y. H. Kim, D. Hesse, M. Alexe, *Nat. Commun.* **2013**, *4*, 2835.
[17] J. E. Spanier, V. M. Fridkin, A. M. Rappe, A. R. Akbashev, A. Polemi, Y. B. Qi, Z. Q. Gu, S. M. Young, C. J. Hawley, D. Imbrenda, G. Xiao, A. L. Bennett-Jackson, C. L. Johnson, *Nat. Photonics* **2016**, *10*, 611.
[18] S. M. Young, A. M. Rappe, *Phys. Rev. Lett.* **2012**, *109*, 116601.
[19] S. M. Young, F. Zheng, A. M. Rappe, *Phys. Rev. Lett.* **2012**, *109*, 236601.
[20] D. Lee, S. H. Baek, T. H. Kim, J. G. Yoon, C. M. Folkman, C. B. Eom, T. W. Noh, *Phys. Rev. B* **2011**, *84*, 125305.
[21] Z. Zhang, P. Wu, L. Chen, J. Wang, *Appl. Phys. Lett.* **2010**, *96*, 232906.
[22] S. Wu, X. Luo, S. Turner, H. Peng, W. Lin, J. Ding, A. David, B. Wang, G. Van Tendeloo, J. Wang, T. Wu, *Phys. Rev. X* **2013**, *3*, 041027.
[23] M. Yang, A. Bhatnagar, M. Alexe, *Adv. Electron. Mater.* **2015**, *1*, 1500139.
[24] X. Y. Chen, T. Yu, F. Gao, H. T. Zhang, L. F. Liu, Y. M. Wang, Z. S. Li, Z. G. Zou, *Appl. Phys. Lett.* **2007**, *91*, 022114.
[25] W. Ji, K. Yao, Y. F. Lim, Y. C. Liang, A. Suwardi, *Appl. Phys. Lett.* **2013**, *103*, 062901.
[26] D. W. Cao, Z. J. Wang, Nasori, L. Y. Wen, Y. Mi, Y. Lei, *Angew. Chem., Int. Ed.* **2014**, *53*, 11027.
[27] S. Cho, J. W. Jang, W. R. Zhang, A. Suwardi, H. Y. Wang, D. W. Wang, J. L. MacManus-Driscoll, *Chem. Mater.* **2015**, *27*, 6635.
[28] L. T. Quynh, C. N. Van, Y. Bitla, J. W. Chen, T. H. Do, W. Y. Tzeng, S. C. Liao, K. A. Tsai, Y. C. Chen, C. L. Wu, C. H. Lai, C. W. Luo, Y. J. Hsu, Y. H. Chu, *Adv. Energy Mater.* **2016**, *6*, 18.
[29] Q. Liu, Y. Zhou, L. You, J. L. Wang, M. R. Shen, L. Fang, *Appl. Phys. Lett.* **2016**, *108*, 022902.
[30] G. C. Xie, K. Zhang, B. D. Guo, Q. Liu, L. Fang, J. R. Gong, *Adv. Mater.* **2013**, *25*, 3820.
[31] Q. J. Xiang, J. G. Yu, M. Jaroniec, *Chem. Soc. Rev.* **2012**, *41*, 782.
[32] Y. H. Ng, A. Iwase, A. Kudo, R. Amal, *J. Phys. Chem. Lett.* **2010**, *1*, 2607.
[33] S. X. Qu, M. H. Li, L. X. Xie, X. Huang, J. G. Yang, N. Wang, S. F. Yang, *ACS Nano* **2013**, *7*, 4070.
[34] A. C. Ferrari, J. Robertson, *Phys. Rev. B* **2000**, *61*, 14095.
[35] M. K. Singh, H. M. Jang, S. Ryu, M. H. Jo, *Appl. Phys. Lett.* **2006**, *88*, 042907.
[36] J. Liu, L. Fang, F. G. Zheng, S. Ju, M. R. Shen, *Appl. Phys. Lett.* **2009**, *95*, 022511.
[37] T. G. Xu, L. W. Zhang, H. Y. Cheng, Y. F. Zhu, *Appl. Catal., B* **2011**, *101*, 382.
[38] S. J. A. Moniz, R. Quesada-Cabrera, C. S. Blackman, J. W. Tang, P. Southern, P. M. Weaver, C. J. Carmalt, *J. Mater. Chem. A* **2014**, *2*, 2922.
[39] J. L. Xie, C. X. Guo, P. P. Yang, X. D. Wang, D. Y. Liu, C. M Li, *Nano Energy* **2017**, *31*, 28.

[40] Y. L. Huang, W. S. Chang, C. N. Van, H. J. Liu, K. A. Tsai, J. W. Chen, H. H. Kuo, W. Y. Tzeng, Y. C. Chen, C. L. Wu, C. W. Luo, Y. Hsua, Y. H. Chu, *Nanoscale* **2016**, *8*, 15795.
[41] R. Maruyama, W. Sakamoto, I. Yuitoo, T. Takeuchi, K. Hayashi, T. Yogo, *Jpn. J. Appl. Phys.* **2016**, *55*, 10TA14.
[42] S. Wang, D. Chen, F. Niu, N. Zhang, L. S. Qin, Y. X. Huang, *RSC Adv.* **2016**, *6*, 34574.
[43] S. Li, J. Zhang, M. G. Kibria, Z. Mi, M. Chaker, D. Ma, R. Nechache, F. Rosei, *Chem. Commun.* **2013**, *49*, 5856.
[44] Q. Li, B. D. Guo, J. G. Yu, J. R. Ran, B. H. Zhang, H. J. Yan, J. R. Gong, *J. Am. Chem. Soc.* **2011**, *133*, 10878.
[45] L. W. Zhang, C. Y. Lin, V. K. Valev, E. Reisner, U. Steiner, J. J. Baumberg, *Small* **2014**, *10*, 3970.
[46] P. Yilmaz, D. Yeo, H. Chang, L. Loh, S. Dunn, *Nanotechnology* **2016**, *27*, 345402.
[47] L. Zhao, L. Fang, W. Dong, F. G. Zheng, M. R. Shen, *Appl. Phys. Lett.* **2013**, *102*, 121905.
[48] X. Wang, L. J. Zhi, K. Mullen, *Nano Lett.* **2008**, *8*, 323.
[49] Q. P. Luo, X. Y. Yu, B. X. Lei, H. Y. Chen, D. B. Kuang, C. Y. Su, *J. Phys. Chem. C* **2012**, *116*, 8111.
[50] J. Zhang, J. G. Yu, M. Jaroniec, J. R. Gong, *Nano Lett.* **2012**, *12*, 4584.
[51] W. S. Hummers, R. E. Offeman, *J. Am. Chem. Soc.* **1958**, *80*, 1339.
[52] P. G. Ren, D. X. Yan, X. Ji, T. Chen, Z. M. Li, *Nanotechnology* **2011**, *22*, 055705.
[53] T. N. Zhou, F. Chen, K. Liu, H. Deng, Q. Zhang, J. W. Feng, Q. Fu, *Nanotechnology* **2011**, *22*, 045704.
[54] M. Zhang, C. X. Jiang, W. Dong, F. G. Zheng, L. Fang, X. D. Su, M. R. Shen, *Appl. Phys. Lett.* **2013**, *103*, 102902.

Received: October 14, 2016
Revised: January 10, 2017
Published online:

